Dual visible/NIR emission from organometallic iridium(III) complexes

Kaitlin A. Phillips [a], Thomas M. Stonelake [a], Peter N. Horton [b], Simon J. Coles [b], Andrew J. Hallett [c], Sean P. O'Kell [c], Joseph M. Beames [a, **], Simon J.A. Pope [a, *]

[a] School of Chemistry, Main Building, Cardiff University, Museum Avenue, Cardiff, CF10 3AT, United Kingdom
[b] UK National Crystallographic Service, Chemistry, Faculty of Natural and Environmental Sciences, University of Southampton, Highfield, Southampton, England, SO17 1BJ, United Kingdom
[c] STG Aerospace, Brecon House, Cwmbran, NP44 3AB, United Kingdom

A B S T R A C T

A series of four substituted benzo[g]quinoxaline species have been synthesised and utilised as cyclo-metalating ligands for iridium(III). The ligands (**L1-L4**) were synthesised and isolated in good yield following the condensation of 2,3-diaminonaphthalene with benzil and three of its derivatives. The substituent modulated electronic properties of **L1-L4** were dominated by intraligand $\pi-\pi^*$ transitions, with the fluorescence profile demonstrating vibronic features attributed to the highly conjugated nature of the chromophore. Iridium(III) complexes of the form [Ir(**L**)$_2$(bipy)]PF$_6$ were synthesised from **L1-L4** in two steps. The electronic properties of the complexes reveal absorption in the UV-vis. region with spin forbidden metal-to-ligand charge transfer (MLCT) transitions possibly contributing at longer wavelengths to ca. 600 nm. Steady state luminescence (aerated, room temperature) on solutions of the complexes showed dual emissive properties in the visible and near-infra red (NIR) regions. Firstly, a vibronically structured emission in the visible region (ca. 525 nm) was attributed to ligand centred fluorescence (lifetime < 10 ns). Secondly, a broad emission peak in the NIR (ca. 950 nm) which extended to around 1200 nm was observed with corresponding lifetimes of 116–162 ns, indicative of triplet excited state emission.

1. Introduction

The development and study of molecular species that are luminescent in the near-infra red (NIR) region continues to attract significant attention. Such studies have been motivated by the many applications (some postulated, others realised) that can benefit from NIR luminescent materials [1]. A range of optoelectronic devices can utilise NIR wavelengths. In the realm of bio-imaging, it has long been argued that the use of fluorescence microscopy as a research and diagnostic tool can greatly benefit from the use of NIR excitation and emission wavelengths [2]. The optical properties of biological tissue are such that its relative transparency in parts of the NIR region can greatly improve optical imaging potential. Achieving NIR luminescence from molecular species has therefore become an ongoing challenge. From a photophysical perspective, consideration of the nature of the excited emitting state and suppression of non-radiative deactivation pathways (particularly where the energy gap between the ground and excited state is small) is a key challenge.

Lanthanide coordination compounds have been successfully developed in this regard with Nd(III), Er(III) and Yb(III) species demonstrating long-lived emission in the 880–1550 nm window [3]. Uniquely, such species possess metal centred (4f) excited states that can give rise to NIR emission. Whilst demonstrating attractive emission properties, the limiting aspect of such systems is overcoming the inherently poor molar absorption coefficients associated with 4f-4f transitions [4]. Over the last two decades a wide range of functionalised ligand systems have been developed to address these challenges [5].

In contrast, only a relatively small number of reports have described NIR emission from d-metal complexes. Most commonly such observations are often defined at low temperature (*i.e.* in a frozen matrix) or under deoxygenated conditions. Of course, both approaches seek to minimise non-radiative quenching of the excited emitting state. For several decades, Cr(III) complexes have

* Corresponding author.
** Corresponding author.
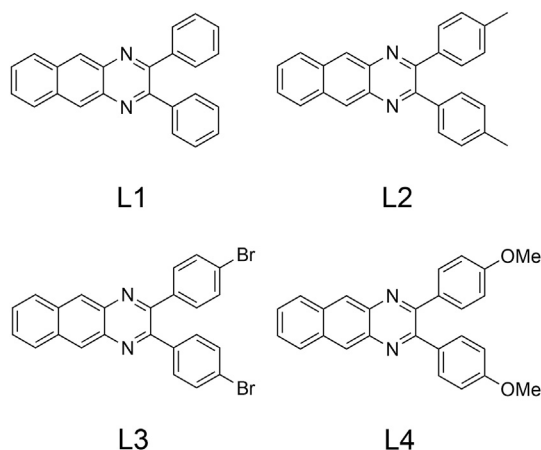*E-mail addresses:* beamesj@cardiff.ac.uk (J.M. Beames), popesj@cardiff.ac.uk (S.J.A. Pope).

been known to demonstrate emission from a *d*-centred excited state (^{2}E) which typically emits around 780 nm, and work continues to maximise these properties [6]. A small number of Ru(II) [7], Os(II) [8], and Pt(II) [9] complexes have also been reported to demonstrate luminescence in the NIR region. Strategies can include lowering the energy of charge transfer (CT) excited states or facilitating the population of low-lying ligand-centred triplet states through efficient spin orbit coupling (SOC) facilitated by the heavy metal atom of the complex.

Cyclometalated Ir(III) complexes have also, very recently, been investigated in this context. Neutral Ir(III) complexes based on 1-(benzo[*b*]thiophen-2-yl)-isoquinolinate show emission between 680 and 850 nm and have been successfully processed into phosphorescent organic light-emitting devices [10]. Ir(III) complexes with boron-dipyrromethane (BODIPY) conjugated ligands have shown interesting NIR absorption and emission properties with particularly long triplet state lifetimes [11]. Wong and co-workers have demonstrated highly tuneable emission properties for Ir(III) complexes using both conjugation and substitution strategies on the cyclometalating ligands [12]. This has allowed the emission to be tuned in the range 420−729 nm with successful application shown within light emitting diodes. Two further reports of cationic Ir(III) complexes that incorporate benzo[*g*]quinoxaline cyclometalated ligands have been previously described by Chen et al. [13] and Sun and co-workers [14]. The extended conjugation of these ligands, *versus* the red wavelength emission observed from previous studies on 2-phenylquinoxaline analogues [15], appears to bathochromically shift the emission wavelength into the NIR region. Building on these reports, we herein describe a further series of Ir(III) organometallic complexes based on substituted benzo[*g*] quinoxaline ligands, providing further evidence that these species are viable NIR emitters, even under ambient conditions (room temperature, aerated solution).

2. Results and discussion

2.1. Synthesis and characterisation

The ligands (**L1-L4**) were synthesised in a single step by the condensation reaction of 2,3-diaminonaphthalene with a benzil derivative in the presence of acetic acid. The ligands (Scheme 1) were isolated in good yield and characterised using a range of analytical and spectroscopic techniques. All relevant data is presented in the experimental section. Good quality single crystals

were obtained for the dibromo-substituted derivative **L3** following slow evaporation of a concentrated chloroform solution. The orange blade shaped crystals were submitted to diffraction studies and the structure was refined in the P2$_1$/n space group and there is a single molecule in the asymmetric unit. The data confirmed the proposed structure (Figs. 1 and 2), with a packing arrangement supported by some long range intermolecular π-π interactions.

The complexes (Scheme 2) were synthesised according to the well known Nonoyama route [16] that first isolates the chloro-bridged dimeric Ir(III) species, [(L)$_2$Ir-(μ-Cl$_2$)-Ir(L)$_2$]. Subsequent splitting of the dimer with 2,2′-bipyridine gave the target cationic complexes. HRMS data was obtained for each of the complexes and showed the correct isotopic distribution in all cases (Fig. 3). In addition to this, ^{1}H NMR spectroscopy was particularly insightful for the determination of the coordination of the ligands to the iridium centre. This was typically noted by the upfield shift of the
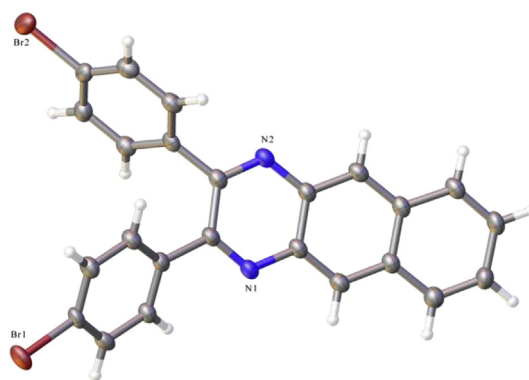

Fig. 1. X-ray crystal structure of **L3**. Ellipsoids are drawn at a 50% probability. Crystal Data: $C_{24}H_{14}Br_2N_2$, $M_r = 490.19$, monoclinic, P2$_1$/n (No. 14), a = 5.7963(2) Å, b = 21.8021(9) Å, c = 15.1661(6) Å, $\beta = 91.211(3)°$, $\alpha = \gamma = 90°$, $V = 1916.15(13)$ Å^3, $T = 100(2)$ K, $Z = 4$, $Z' = 1$, $\mu(MoK_\alpha) = 4.243$ mm^{-1}, 19907 reflections measured, 4396 unique ($R_{int} = 0.0501$) which were used in all calculations. The final wR_2 was 0.1219 (all data) and R_1 was 0.0491 (I > 2(I)).
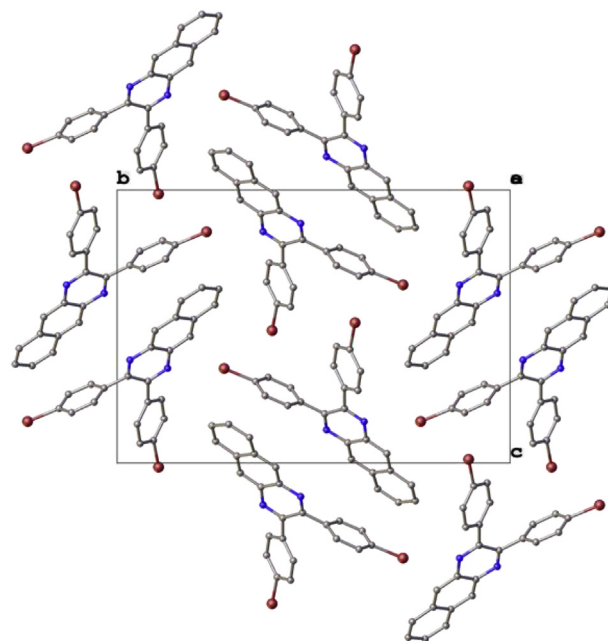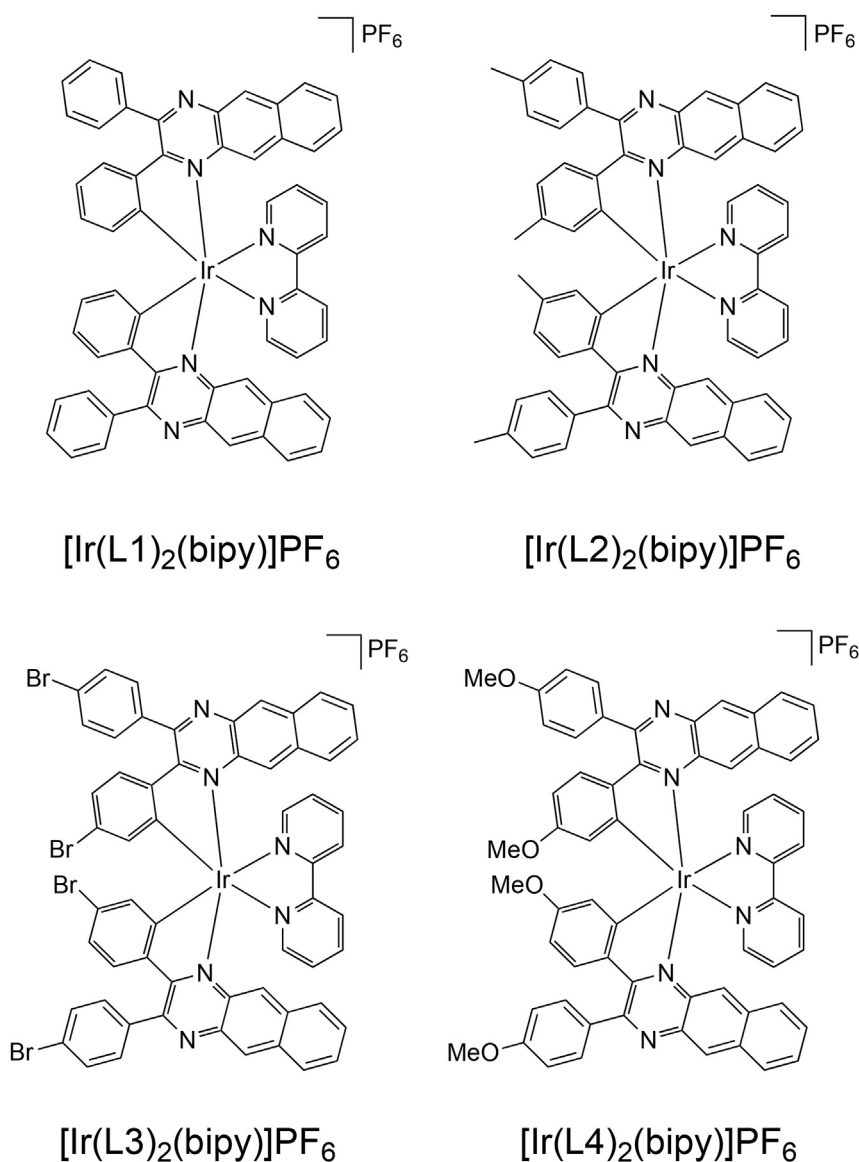

Fig. 2. Packing diagram for **L3** obtained from the X-ray crystal structure. Ellipsoids are drawn at a 50% probability.

Scheme 1. The benzo[*g*]quinoxaline ligands synthesised in this study for Ir(III) complexation.

Scheme 2. The structures of the iridium(III) complexes synthesised in this study.

proton adjacent to the cyclometalating carbon atom (for example, Fig. 4). In the ^{1}H NMR spectra of [Ir(**L2**)$_2$(bipy)]PF$_6$ and [Ir(**L4**)$_2$(bipy)]PF$_6$, there were two unique methyl environments (note that they are equivalent in the free ligand) indicative of cyclometalation in the expected manner (*i.e.* the benzo[*g*]quinoxaline ligands do not act in a bridging manner). The frequency separations in these inequivalent methyl resonances was approximately 0.5 ppm.

2.2. UV-vis. and luminescence spectroscopy

The solution state absorption spectra of the ligands **L1**-**L4** (Fig. 5) were recorded as chloroform solutions at 1×10^{-5} M and were comparable to related literature examples that are based on the benzo[*g*]quinoxaline chromophore [11—13]. All ligands showed strong $(\varepsilon > 10^4 \, M^{-1}cm^{-1})$ $\pi-\pi^*$ transitions in the UV region at 200—400 nm. A shoulder feature extended beyond 450 nm but again is attributed to low energy $\pi-\pi^*$ transitions although weaker $n-\pi^*$ transitions may also contribute in this region. The phenyl substituent (-H, -Me, -Br, -OMe) of the ligand clearly influences the positioning of these bands, with the methoxy substituted **L4**

possessing the most bathochromically shifted features, which was attributed to the increased conjugation induced by the -OMe substituents. The corresponding emission spectra obtained for these ligands shows that they are all luminescent in the visible region from 400 to 550 nm showing some vibronic structure to the peak shape. Again the nature of the substituent influences the peak positioning, and in this case the benzil derivative (**L1**) possesses the longest emission wavelength. The recorded lifetimes for each ligand were found to be < 5 ns, consistent with fluorescence from a $^1\pi-\pi^*$ emitting state.

UV-vis. spectroscopy on solutions of the complexes revealed spectra with multiple contributions across the UV and visible regions (Fig. 6; Table 1). The majority of peaks at wavelengths than 250—450 nm are attributed to different ligand-centred transitions that are perturbed upon coordination to the Ir(III) centre, as well as contributions from spin allowed metal-to-ligand charge transfer bands (^{1}MLCT).

The ancillary bipyridine ligand $\pi-\pi^*$ absorptions are also likely to contribute ca. 270—290 nm. When compared to the ligand spectra, each of the complexes showed additional absorption bands
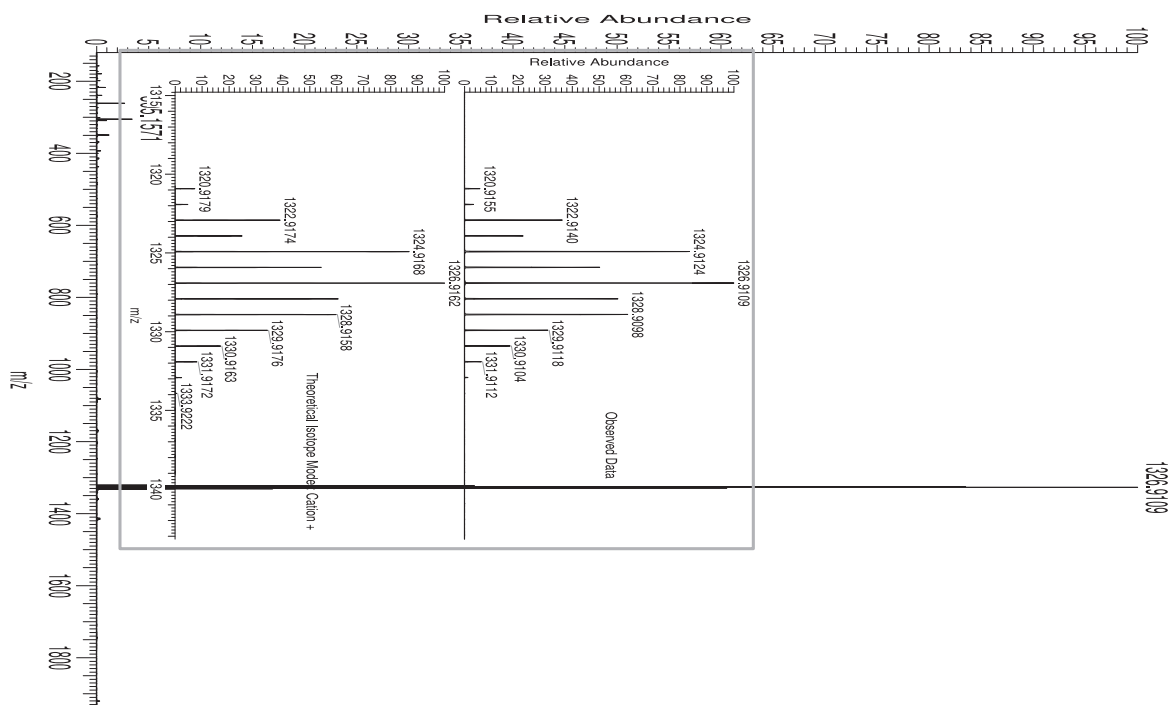
Fig. 3. Example of a high resolution mass spectrum obtained for [Ir(**L3**)$_2$(bipy)]PF$_6$ showing the cationic fragment (main) and observed *versus* theoretical isotopic distribution pattern (inset).

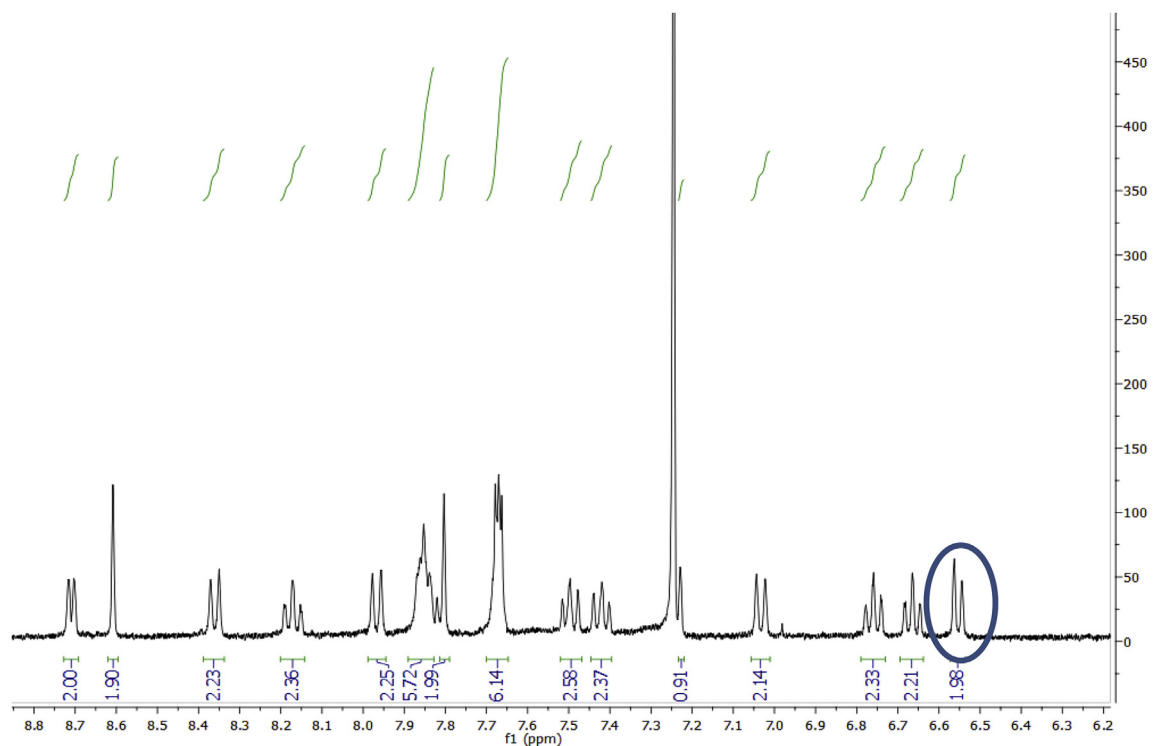**Fig. 4.** ^{1}H NMR spectrum of [Ir(**L1**)$_2$(bipy)]PF$_6$ that shows the upfield shift of the ligand proton adjacent to the cyclometalating carbon atom.

across the visible region that extended >600 nm. These weaker absorption bands may comprise spin forbidden ^{3}MLCT bands [17]. These Ir(III) complexes therefore demonstrate strong bathochromic shifts in the visible region relative to related complexes based upon substituted 2-phenylquinoxaline ligands [15]. This is attributed to

the lowering of the MLCT transitions due to the added conjugation of the ligand benzo[g]quinoxaline ligands. The subtle variation between the complexes are again indicative of the electronic character of the substituents; as with the free ligands the methoxy-substituted variant [Ir(**L4**)$_2$(bipy)]PF$_6$ possessed the lowest energy
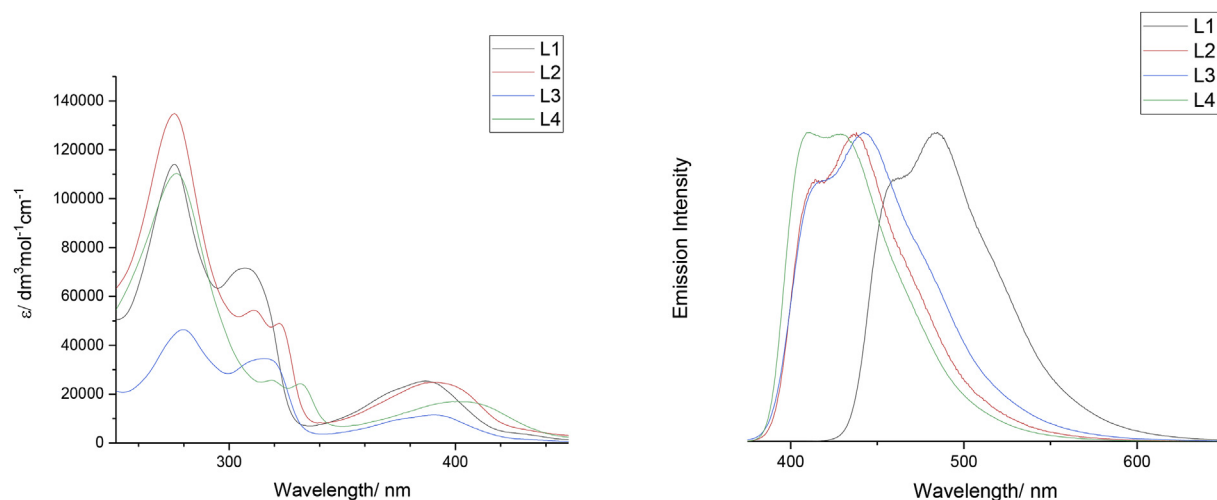
Fig. 5. UV—vis absorption (left) and emission (right) spectra of the ligands (10^{-5} M CHCl$_3$).

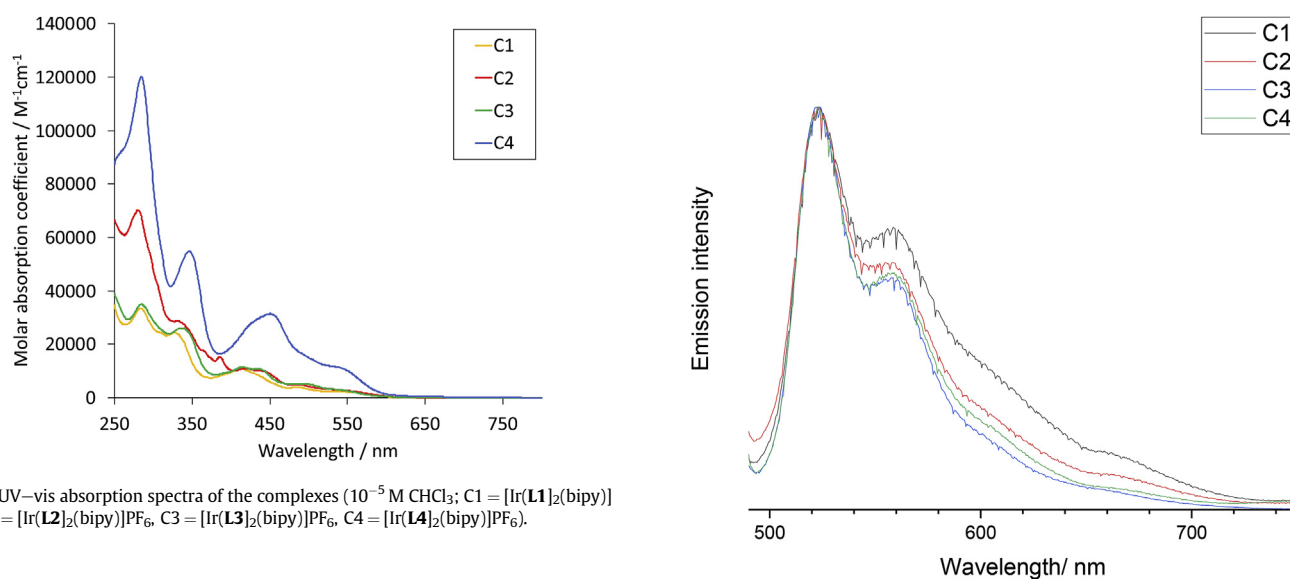**Fig. 6.** UV—vis absorption spectra of the complexes (10^{-5} M CHCl$_3$; C1 = [Ir(**L1**)$_2$(bipy)] PF$_6$, C2 = [Ir(**L2**)$_2$(bipy)]PF$_6$, C3 = [Ir(**L3**)$_2$(bipy)]PF$_6$, C4 = [Ir(**L4**)$_2$(bipy)]PF$_6$).

Fig. 7. Visible emission spectra for the complexes (aerated CHCl$_3$, $\lambda_{exc} = 405$ nm; C1 = [Ir(**L1**)$_2$(bipy)]PF$_6$, C2 = [Ir(**L2**)$_2$(bipy)]PF$_6$, C3 = [Ir(**L3**)$_2$(bipy)]PF$_6$, C4 = [Ir(**L4**)$_2$(-bipy)]PF$_6$).

absorption features.

The luminescence spectra for the complexes were recorded on aerated samples at room temperature (Table 1). In all cases an excitation wavelength of 470 nm was used as this corresponds to strong absorption bands in all of the complexes reported herein. The first collection of emission spectra were recorded between 490 and 750 nm and revealed a defined vibronic progression to the peak shape that was reproduced for each of the four complexes, but differentiated from the corresponding free ligands (Fig. 7). In fact these emission spectra for the complexes are virtually superimposable, with little variance in the wavelength positioning of these

bands across the series. Time-resolved measurements provided the emission lifetimes for the visible emission which were all short-lived (<10 ns). Taken together the data implies that these features may be due to intraligand transitions associated with the coordinated phenyl benzo[g]quinoxaline units (see further discussion in computational section).

Table 1
Absorption and emission data for the ligands and complexes.[a] Recorded in aerated CHCl$_3$;[b] $\lambda_{exc} = 405$ nm;[c] $\lambda_{exc} = 295$ nm;[d] $\lambda_{exc} = 505$ nm;[e] $\lambda_{exc} = 355$ nm.

Compound	λ_{abs}/nm[a]	λ_{em}/nm[a,b] (τ/ns[c])	λ_{em}/nm[a,d] (τ/ns[e])
L1	386, 309, 276	485 (1.4)	—
L2	391, 323, 312, 276	480 (1.1)	—
L3	393, 318, 280	490 (1.8)	—
L4	402, 332, 319, 276	480 (1.1)	—
[Ir(**L1**)$_2$(bipy)]PF$_6$	554sh, 490, 415, 329, 286	520 (4.9)	915 (119)
[Ir(**L2**)$_2$(bipy)]PF$_6$	554sh, 491, 445, 420, 388, 367, 334, 283	520 (7.0)	912 (148)
[Ir(**L3**)$_2$(bipy)]PF$_6$	554sh, 500, 439, 415, 340, 287	520 (2.9)	928 (116)
[Ir(**L4**)$_2$(bipy)]PF$_6$	554sh, 455, 348, 285	520 (<1)	949 (162)

Interestingly, these observations do not correspond with the luminescence properties of closely related 2-phenylquinoxaline complexes of Ir(III), which we have previously described [15], which were shown to be phosphorescent around 620–650 nm and attributed to a ^{3}MLCT emitting state. Therefore, further luminescence studies on the complexes investigated the possibility of emission in the NIR region. Again, aerated solutions were studied at room temperature and, using an excitation wavelength of 505 nm, spectra were collected between 850 and 1300 nm.

As shown in Fig. 8, under these conditions, each of the complexes demonstrated luminescence in the NIR region peaking around 915–950 nm. The appearance of the emission peak is very broad and tails to ca. 1250 nm. This is consistent with the findings of previous work on related complex structures using different benzo[g]quinoxaline based ligands [12,13]. Each of the spectra includes an additional sharp emission peak centred at 1274 nm which is characteristic of the radiative decay that accompanies the spin forbidden relaxation of singlet oxygen ($^1O_2 \rightarrow {}^3O_2$). The photogeneration of singlet oxygen in solution, firstly corroborates the use of aerated solvent for the measurements, and secondly, implies the presence of an excited triplet state on a sensitizer molecule. Further, time-resolved measurements monitoring the decay kinetics of the NIR emission band revealed emission lifetimes in the range of 116–162 ns, each indicative of a triplet excited state. Critically, these lifetimes are significantly longer than those attributed to the visible emission of the complexes (measured under identical sample conditions).

2.3. Density functional theory (DFT) calculations

The geometries of all the complexes were optimised in Gaussian09 using the B3LYP functional with a combination of 6-31G* basis sets for the ligand atoms and the Stuttgart-Dresden (SDD) core potential/basis set for the iridium metal core [18]. Solvent effects were included implicitly using the self-consistent reaction field (SCRF) and polarized continuum (IEFPCM) models. Time dependent DFT (TD-DFT) calculations were performed on the stationary points to determine the first five singlet excited states for each complex, using the same basis sets and the long range corrected CAM-B3LYP functional. Phosphorescence and spin forbidden absorption bands were computed using unrestricted DFT calculations, computing parameters for the first triplet state of the complexes (T_1). Fig. 8 shows the superimposition of the calculated molecular geometries of the complexes in both singlet and triplet excited states. Whilst the geometries look broadly similar it is notable that there are differing degrees of distortion within the coordinated ligand fragments of the two excited states. The composition of the complexes' HOMOs and LUMOs are detailed in Table 2.

In all cases the cyclometalated ligands are predicted to contribute strongly to both molecular orbitals, with Ir contributions of 13–26% for the HOMO. Orbital contributions to the excited states (see ESI) show that a range of transitions are predicted for each. The lowest calculated energy excited state is dominated by the HOMO → LUMO transition, which may comprise both MLCT and intra(-cyclometalated)ligand contributions (Table 2). It is noteworthy that the DFT calculations suggest that bipyridine localised orbitals primarily contribute to the upper lying LUMO+2 and LUMO+3, neither of which feature strongly as participants in contributing transitions to the predicted excited states. Ligand centred transitions, more specifically transitions localised on the benzo[g]quinoxaline ligands, are assigned as the dominant contributors to the visible complex emission. This is consistent with the similarity in vibronic band shapes between the free ligand emission (Fig. 2) and the complex emission band (Fig. 3). Both of these emission bands show clear vibrational progressions, with a vibrational spacing of ~1300 cm^{-1}. This vibrational frequency is consistent with quinoxalene (predominantly pyrazine) ring breathing modes, which are the most infrared active modes for these ligands. The electronic emission spectrum of the free ligand has been simulated using the Franck-Condon-Herzberg-Teller approach implemented in the Gaussian09 software package [19,20]. Both ground and excited states have been optimised using the DFT//B3LYP/6-31G(d) method, with the excited state being optimised using TD-DFT. The Franck-Condon progression has then been calculated using the vibrational frequencies from the two states, at a temperature of 300 K, and convoluted with a HWHM of 500 cm^{-1}. The computed spectrum is shown below (Fig. 9) in comparison with the experimental spectra of the free ligand **L1**, and the complex [Ir(**L1**)$_2$(bipy)]PF$_6$.

The spectra shown in Fig. 9 show remarkable agreement between simulation and experiment. The simulated spectrum has been deliberately slightly under convoluted to highlight the overlap of the vibronic peak positions. This agreement not only confirms the assignment of the vibronic features, but further illustrates the similarity between **L1** within the complex [Ir(**L1**)$_2$(bipy)]PF$_6$ and as its free ligand. The vibrational spacing is approximately consistent between the free ligand and the complex, but there is a clear change in the Franck-Condon factors associated with the progression. This is equally consistent with the assignment: the metal binding to the ligand alters the bond lengths of the pyrazine ring, slightly lengthening the C-N bonds (C=N, 1.315 Å; C-N, 1.37 Å in the free ligand, C=N, 1.347 Å; C-N, 1.39 Å in the complex) which will alter the Franck-Condon overlap between S_0 and S_1.

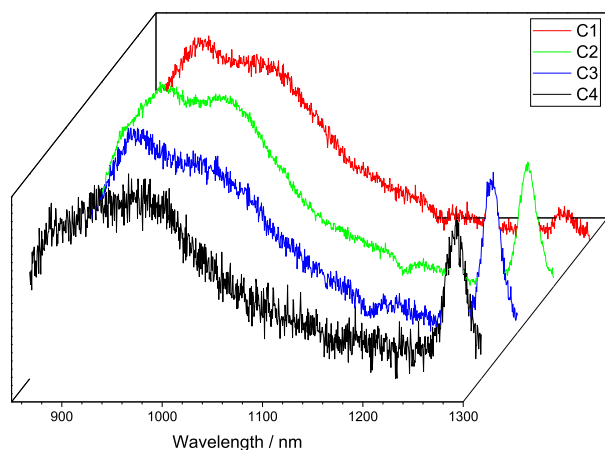Further photochemical properties of the complexes have also

Fig. 8. Steady state near-IR emission spectra of the complexes. The peak at 1274 nm is due to the photogeneration of, and subsequent emission from, $^1O_2$. (Aerated CHCl$_3$, λ_{exc} = 505 nm; C1 = [Ir(**L1**)$_2$(bipy)]PF$_6$, C2 = [Ir(**L2**)$_2$(bipy)]PF$_6$, C3 = [Ir(**L3**)$_2$(bipy)]PF$_6$, C4 = [Ir(**L4**)$_2$(bipy)]PF$_6$).

Table 2
Predicted MO compositions of the HOMO and LUMO of the complexes.

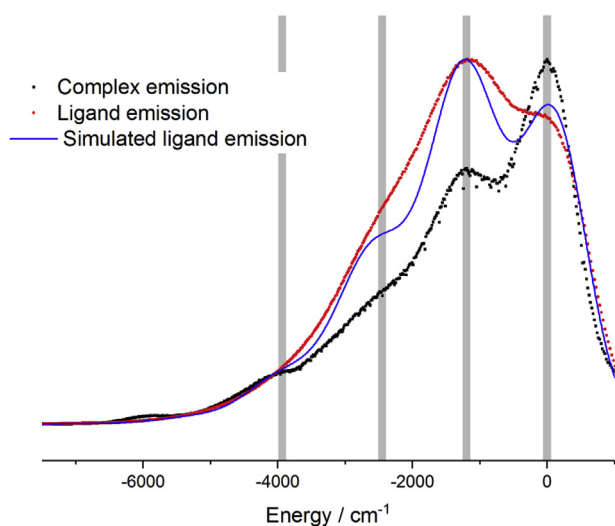| Compound [a]	Ir (5d)	C^N (1)	C^N (2)	bipy
		HOMO		
[Ir(**L1**)$_2$(bipy)]PF$_6$	26%	36%	36%	1%
[Ir(**L2**)$_2$(bipy)]PF$_6$	26%	37%	36%	1%
[Ir(**L3**)$_2$(bipy)]PF$_6$	13%	44%	42%	0%
[Ir(**L4**)$_2$(bipy)]PF$_6$	16%	40%	43%	1%
		LUMO		
[Ir(**L1**)$_2$(bipy)]PF$_6$	3%	48%	47%	1%
[Ir(**L2**)$_2$(bipy)]PF$_6$	3%	47%	48%	2%
[Ir(**L3**)$_2$(bipy)]PF$_6$	3%	49%	46%	3%
[Ir(**L4**)$_2$(bipy)]PF$_6$	3%	47%	49%	2%

Fig. 9. Franck-Condon simulation of the **L1** A-X transition (blue), overlaid against the experimental emission spectra of the free ligand **L1** (red), and the complex **[Ir(L1)₂(-bipy)]PF₆** (black). The spectra have been offset by their respective vibronic origin, and are therefore displayed as emission energy (cm^{-1}) relative to zero. The grey bars are a guide to the eye, showing different vibronic features. (For interpretation of the references to colour in this figure legend, the reader is referred to the Web version of this article.)

been computed: the wavelengths of selected calculated transitions are shown in Table 3, including those that are spin forbidden and thus relate to an excitation ($T_1 \leftarrow S_0$, at S_0 minimum energy geometry) and phosphorescence ($T_1 \rightarrow S_0$, at T_1 minimum energy geometry). The overlap between the S_1 and T_1 minimum energy geometries are highlighted in Fig. 10. The calculated data

Table 3
Calculated vertical transitions for the complexes.

Compound	$S_1 \leftarrow S_0$/nm	$T_1 \leftarrow S_0$/nm	$T_1 \rightarrow S_0$/nm
[Ir(**L1**)₂(bipy)]PF₆	433	557	993
[Ir(**L2**)₂(bipy)]PF₆	434	602	980
[Ir(**L3**)₂(bipy)]PF₆	428	590	1019
[Ir(**L4**)₂(bipy)]PF₆	428	583	962

corresponds well with the experimental results and importantly predicts that the emission should occur in the NIR region around 962—1019 nm. Both the spin allowed and spin forbidden excitations correlate well with the primary features of the complexes' absorption spectra. The DFT results suggest that the variations in ligand structure induce differences in emission energy, but these subtleties were not apparent in the broadened features of the experimental data. It is also intriguing to see that such subtle changes in geometry within the triplet state, i.e. geometric relaxation after ISC, lead to dramatic changes in the $T_1 - S_0$ energy gap. Tempering or expanding upon this shift will form the basis of future work.

3. Conclusion

Extending the conjugation of cyclometalating ligands on iridium(III) can bathochromically shift luminescence from organometallic complexes into the NIR spectral region. For Ir(III), substituted benzo[*g*]quinoxaline type cyclometalting ligands are appropriate choices to achieve this and the study shows that supporting DFT calculations can reliably predict the spin forbidden transitions that dominate the lowest energy absorptions and phosphorescent emission properties of these complexes.

4. Experimental

All reactions were performed with the use of vacuum line and Schlenk techniques. Reagents were commercial grade and were used without further purification. ^{1}H and ^{13}C{^{1}H} NMR spectra were run on NMR-FT Bruker 400 or 250 spectrometers and recorded in CDCl₃. ^{1}H and ^{13}C-{^{1}H} NMR chemical shifts (δ) were determined relative to internal TMS and are given in ppm. Low-resolution mass spectra were obtained by the staff at Cardiff University. High-resolution mass spectra were carried out by at the EPSRC National Mass Spectrometry Service at Swansea University. UV-Vis studies were performed on a Jasco V-570 spectrophotometer as MeCN solutions (10^{-5} M). Photophysical data were obtained on a JobinYvon-Horiba Fluorolog spectrometer fitted with a JY TBX picosecond photodetection module as MeCN solutions. A Hamamatsu R5509-73 detector (cooled to $-80\,^{\circ}$C using a C9940 housing) was used for NIR luminescence measurements. For the NIR lifetimes the pulsed laser source was a Continuum Minilite Nd:YAG
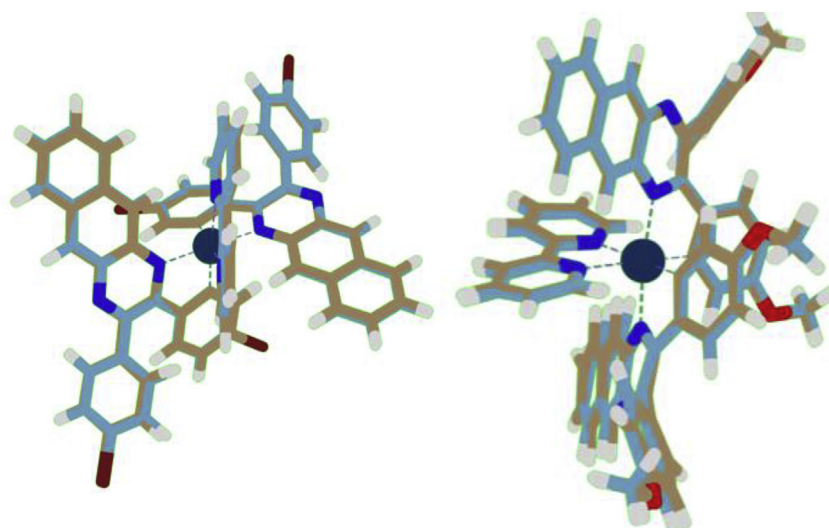

Fig. 10. A comparison of the calculated geometries of the singlet and triplet excited states for [Ir(**L3**)₂(bipy)]PF₆ (left, RMSD = 0.185 Å) and [Ir(**L4**)₂(bipy)]PF₆ (right, RMSD = 0.149 Å).

configured for 355 nm output. For all NIR emission data, a 850 nm band pass filter was used. The pulsed source was a Nano-LED configured for 295 nm output operating at 1 MHz. All luminescence lifetime profiles were obtained using the JobinYvon-Horiba FluoroHub single photon counting module and the data fits yielded the lifetime values using the provided DAS6 deconvolution software.

4.1. Data collection and processing

X-ray diffraction datasets were measured on a Rigaku AFC12 diffractometer equipped with enhanced sensitivity (HG) Saturn 724 + CCD detector mounted at the window of an FR-E + SuperBright rotating anode generator (Mo Kα, λ = 0.71075 Å) with VHF Varimax optics (70 μm focus) [21] using CrysAlisPro software [22] for data collection and reduction.

4.2. Structure analysis and refinement

The structures were solved by direct methods using Superflip [23] and refined on F_o^2 by full-matrix least-squares refinements using SHELXL [24] within the OLEX2 suite [25]. All non-hydrogen atoms were refined with anisotropic displacement parameters, and all hydrogen atoms were added at calculated positions and refined using a riding model with isotropic displacement parameters based on the equivalent isotropic displacement parameter (U_{eq}) of the parent atom.

4.3. Density functional theory

The geometries of all the complexes were optimised in Gaussian09 using the B3LYP functional with a combination of 6-31G* basis sets for the ligand atoms and the Stuttgart-Dresden (SDD) core potential/basis set for the iridium metal core [16]. Solvent effects were included implicitly using the self-consistent reaction field (SCRF) and polarized continuum (IEFPCM) models, and in all cases the solvent chosen was chloroform, characterised by an electrical permittivity of $\varepsilon = 4.7113$. Molecular orbital calculations were performed using the same basis sets and functionals, and decomposition analysis was performed on the frontier orbitals using the GaussSum software package. TD-DFT calculations were performed on the stationary points to determine the first five singlet excited states for each complex, using the same basis sets and the long range corrected CAM-B3LYP functional. Phosphorescence and spin forbidden absorption bands were computed using unrestricted DFT calculations, computing parameters for the first triplet state of the complexes (T_1). The Franck-Condon simulations were performed without implicit solvation, however it is clear from the agreement between experiment and theory that this does not significantly alter the results. Additionally, the Franck-Condon progressions are harmonic in nature. Small shifts in peak positions would be expected using anharmonic modes (the harmonic scaling factor for this functional and basis set is ca.0.962) [26], however these shifts are expected to be small relative to the peak widths. The Chimera software package was used to visualise the complexes and compare singlet and triplet geometries [27].

4.4. Synthesis

4.4.1. Synthesis of 2,3-diphenylbenzo[g]quinoxaline (L1)

To a stirred solution of benzil (322 mg, 1.6 mmol) in ethanol (15 mL) was added 2,3-diaminonaphthalene (250 mg, 1.6 mmol) and acetic acid (0.5 mL). The reaction mixture was heated at reflux under a nitrogen atmosphere for 24 h. The reaction mixture was cooled to room temperature and a precipitate collected by filtration

to give L1 as a brown solid (0.34 g, 64%). ^{1}H NMR (300 MHz, CDCl$_3$): δ_H 8.68 (s, 2H, CH), 8.05 (dd, J = 3.21 Hz, 6.39 Hz, 2H), 7.50 (m, 6H), 7.30 (m, 6H) ppm. ^{13}C{^{1}H} NMR (101 MHz, CDCl$_3$): δ_C 154.2, 139.2, 138.0, 134.1, 129.8, 129.0, 128.6, 128.3, 127.6, 126.8 ppm. HRMS found m/z 333.1387; calcd m/z 333.1386 for C$_{24}$H$_{16}$N$_2$. UV-vis. (CHCl$_3$) λ_{max} (ε/dm^3 mol^{-1} cm^{-1}): 386 (25200), 309 (71500), 276 (114100) nm. Selected IR (solid) υ_{max} = 1607, 1508, 1441, 1346, 1248, 1175, 1013, 976, 876, 836, 760, 741, 691, 552, 500.0, 490, 467 cm^{-1}.

4.4.2. Synthesis of 2,3-di-p-tolylbenzo[g]quinoxaline (L2)

As L1 but with 4,4′-dimethylbenzil (376 mg, 1.6 mmol) and 2,3-diaminonaphthalene (250 mg, 1.6 mmol). Product collected as a brown solid (0.41 g, 71%). ^{1}H NMR (300 MHz, CDCl$_3$) δ_H 8.73 (s, 2H), 8.12 (dd, J = 3.2, 6.5 Hz, 2H), 7.57 (dd, J = 3.1, 6.7 Hz, 2H), 7.49 (d, J = 8.0 Hz, 4H), 7.19 (d, J = 8.0 Hz, 4H), 2.41 (s, 6H) ppm. ^{13}C{^{1}H} NMR (101 MHz, CDCl$_3$) δ_C 154.3, 139.0, 138.0, 136.5, 134.0, 129.8, 129.0, 128.6, 127.4, 126.6, 21.4 ppm. HRMS m/z found 361.1699; calcd m/z 316.1699 for C$_{26}$H$_{20}$N$_2$. UV-vis. (CHCl$_3$) λ_{max} (ε/dm^3 mol^{-1} cm^{-1}): 391 (24800), 323 (48600), 312 (54200), 276 (134500) nm. Selected IR (solid) υ_{max} = 1607, 1508, 1445, 1346, 1247, 1174, 1109, 1013, 972, 878, 835, 819, 760, 559, 500, 490, 471, 421 cm^{-1}.

4.4.3. Synthesis of 2,3-bis(4-bromophenyl)benzo[g]quinoxaline (L3)

As L1 but with 4,4′-dibromobenzil (581 mg, 1.6 mmol) and 2,3-diaminonaphthalene (250 mg, 1.6 mmol). Product collected as a light brown solid (0.56 g, 72%). ^{1}H NMR (400 MHz, CDCl$_3$) δ_H 8.66 (s, 2H), 8.05 (dd, J = 3.2, 6.5 Hz, 2H), 7.52 (m, 2H), 7.46 (d, J = 8.4 Hz, 4H), 7.38 (d, J = 8.4 Hz, 4H) ppm. ^{13}C{^{1}H} NMR (101 MHz, CDCl$_3$) δ_C 152.6, 137.9, 137.8, 134.3, 131.7, 131.4, 128.6, 127.7, 127.0, 123.9 ppm. HRMS found m/z 490.9569; calcd m/z 490.9576 for C$_{24}$H$_{15}$Br$_2$N$_2$. UV-vis. (CHCl$_3$) λ_{max} (ε/dm^{3}mol^{-1}cm^{-1}): 393 (11400), 318 (34300), 280 (46400) nm. Selected IR (solid) υ_{max} = 1605, 1510, 1445, 1344, 1246, 1173, 1109, 1053, 1011, 972, 880, 833, 795, 758, 745, 723, 656, 646, 623, 573, 557, 548, 532, 498, 471, 409 cm^{-1}.

4.4.4. Synthesis of 2,3-bis(4-methoxyphenyl)benzo[g]quinoxaline (L4)

As L1 but with anisil (427 mg, 1.6 mmol) and 2,3-diaminonaphthalene (250 mg, 1.6 mmol). Product collected as a light brown solid (0.50 g, 80%). ^{1}H NMR (300 MHz, CDCl$_3$) δ_H 8.61 (s, 2H, CH), 8.02 (dd, J = 3.01, 6.42 Hz, 2H), 7.48 (d, J = 8.31 Hz, 6H), 6.83 (d, J = 8.43, 4H), 3.78 (s, 6H) ppm. ^{13}C{^{1}H} (101 MHz, CDCl$_3$) δ_C 160.4, 153.8, 138.0, 133.9, 131.8, 131.3, 128.5, 127.2, 126.5, 113.8, 55.4 ppm. HRMS found m/z 393.1593; calcd m/z 392.1598 for C$_{26}$H$_{21}$N$_2$O$_2$. UV-vis. (CHCl$_3$) λ_{max} (ε/dm^{3}mol^{-1}cm^{-1}): 402 (16900), 332 (24200), 319 (25600), 276 (110300) nm. Selected IR (solid) υ_{max} = 1605, 1578, 1541, 1508, 1445, 1414, 1344, 1275, 1246, 1173, 1109, 1051, 1015, 976, 891, 880, 853, 833, 795, 756, 747, 656, 646, 623, 592, 573, 557, 532, 525, 496, 474, 421 cm^{-1}.

4.5. Synthesis of complexes

Synthesis of [Ir(C^N)$_2$Cl$_2$]$_2$ IrCl$_3$. xH$_2$O (1 eq.) and ligand, L (2 eq.) were dissolved in 2-ethoxyethanol (10 mL) and the reaction mixture heated at reflux for 48 h. The reaction was then cooled to room temperature and water (30 mL) was added to form a dark brown precipitate. The solid was collected by filtration to yield [(L)$_2$Ir(μ-Cl$_2$)Ir(L)$_2$].

4.5.1. Synthesis of [Ir(L1)$_2$(bipy)][PF$_6$]

[(L1)$_2$Ir(μ-Cl$_2$)Ir(L1)$_2$] (195 mg, 0.11 mmol) and 2,2′-bipyridyl (36 mg, 0.23 mmol) were dissolved in 2-ethoxyethanol (10 mL) and heated at reflux for 24 h under a nitrogen atmosphere. The reaction mixture was then cooled to room temperature and a saturated

solution of aqueous ammonium hexafluorophosphate was added. Upon formation of a red precipitate, the mixture was filtered and the precipitate washed with water and diethyl ether. The crude solid was purified by column chromatography using DCM followed by DCM/MeOH (9:1). Product collected as first red band with DCM/MeOH and dried in vacuo to give [Ir(**L1**)$_2$(bipy)][PF$_6$] as a red solid (38 mg, 15%). ^{1}H NMR (400 MHz, CDCl$_3$) δ_H 8.65 (d, $J = 5.6$ Hz, 2H), 8.55 (s, 2H), 8.31 (d, $J = 8.8$ Hz, 2H), 8.12 (app. t, $J = 8.8$ Hz, 2H), 7.91 (d, $J = 8.4$ Hz, 2H), 7.89–7.77 (m, 6H), 7.75 (s, 2H), 7.64–7.60 (m, 6H), 7.44 (app. t, $J = 8.8$ Hz, 2H), 7.36 (app. t, $J = 6.4$ Hz, 2H), 7.17 (s, 2H), 6.98 (d, $J = 8.8$ Hz, 2H), 6.70 (app. t, $J = 5.6$ Hz, 2H), 6.61 (app. t, $J = 7.2$ Hz, 2H), 6.50 (d, $J = 7.2$ Hz, 2H) ppm. ^{13}C{^{1}H} NMR (101 MHz, CDCl$_3$) δ_C 164.5, 155.8, 154.3, 153.8, 147.9, 144.3, 139.6, 134.6, 133.7, 132.5, 131.5, 130.4, 129.4, 129.4, 128.9, 128.8, 128.2, 128.0, 127.6, 125.4, 122.0, 119.5, 114.4, 77.4, 76.7 ppm. HRMS found m/z 1011.2777; calcd m/z 1011.2786 for C$_{58}$H$_{38}$IrN$_8$. UV-vis. (CHCl$_3$) λ_{max} (ε/dm^3 mol^{-1} cm^{-1}): 554 (2100), 490 (3900), 415 (10700), 329 (24200), 286 (33200) nm. Selected IR (solid) $\upsilon_{max} = 1607, 1445, 1350, 1253, 835, 760, 738, 696, 574, 557, 500, 468$ cm^{-1}.

4.5.2. Synthesis of [Ir(**L2**)$_2$(bipy)][PF$_6$]

As [Ir(**L1**)$_2$(bipy)][PF$_6$] but with [(**L2**)$_2$Ir(μ-Cl$_2$)Ir(**L2**)$_2$] (56 mg, 0.03 mmol) and 2,2′-bipyridyl (10 mg, 0.07 mmol). Product collected as a red solid (44 mg, 62%) ^{1}H NMR (400 MHz, CDCl$_3$) δ_H 8.67 (d, $J = 6.60$ Hz, 2H), 8.59 (s, 2H), 8.53 (d, $J = 8.8$ Hz, 2H), 8.21 (dd, $J = 7.72, 8.80$ Hz, 2H), 7.98 (d, $J = 8.80$ Hz, 2H), 7.78 (m, 8H), 7.50 (m, 6H), 7.42 (app. t, $J = 7.70$ Hz, 2H), 7.24 (d, $J = 7.72$ Hz, 2H), 7.03 (d, $J = 7.72$ Hz, 2H), 6.65 (d, $J = 8.84$ Hz, 2H), 6.43 (s, 2H), 2.57 (s, 6H), 1.94 (s, 6H) ppm. ^{13}C{^{1}H} NMR (101 MHz, CDCl$_3$) δ_C 164.8, 156.0, 148.0, 142.5, 141.7, 141.1, 140.5, 136.9, 136.3, 135.1, 134.0, 133.4, 132.3, 130.0, 129.1, 128.8, 128.5, 128.1, 128.0, 127.7, 127.5, 125.8, 123.8, 122.0, 21.8, 21.7 ppm. HRMS found m/z 1067.3406; calcd m/z 1067.3413 for C$_{62}$H$_{46}$IrN$_6$. UV-vis. (CHCl$_3$) λ_{max} (ε/dm^{3}mol^{-1} cm^{-1}): 554 (2500), 491 (4900), 445 (9700), 420 (11000), 388 (14900), 367 (16900), 334 (28300), 283 (69500) nm. Selected IR (solid) $\upsilon_{max} = 1586, 1503, 1445, 1398, 1359, 1314, 1257, 1211, 1177, 1138, 1069, 1042, 978, 833, 772, 635, 579, 556, 513, 471, 424, 407$ cm^{-1}.

4.5.3. Synthesis of [Ir(L3)$_2$(bipy)][PF$_6$]

As [Ir(L1)$_2$(bipy)][PF$_6$] but with [(**L3**)$_2$Ir(μ-Cl$_2$)Ir(**L3**)$_2$] (150 mg, 0.06 mmol) and 2,2′-bipyridyl (20 mg, 0.13 mmol). Product collected as a red solid (75 mg, 61%). ^{1}H NMR (400 MHz, CDCl$_3$) δ_H 8.82 (d, $J = 8.80$ Hz, 2H), 8.56 (s, 2H), 8.52 (d, $J = 6.40$ Hz, 2H), 8.21 (app. t, $J = 8.40$ Hz, 2H), 7.94 (d, $J = 7.20$ Hz, 3H), 7.77–7.68 (m, 5H), 7.62 (s, 2H), 7.49 (app. t, $J = 8.40$ Hz, 3H), 7.39 (app. t, $J = 6.00$ Hz, 3H), 7.11 (d, $J = 7.20$ Hz, 3H), 6.97 (m, 5H), 6.62 (s, 2H) ppm. ^{13}C{^{1}H} NMR (101 MHz, d6-acetone) δ_C 164.5, 155.8, 153.4, 149.6, 144.1, 141.0, 138.8, 137.5, 137.4, 136.8, 134.1, 133.7, 133.6, 132.3, 131.5, 129.3, 129.1, 128.5, 128.3, 127.9, 127.5, 126.5, 126.0, 124.8, 124.2, 122.4, 78.3 ppm. LRMS found m/z 1326.90; calcd m/z 1326.92 for C$_{58}$H$_{34}$Br$_4$IrN$_6$. UV-vis. (CHCl$_3$) λ_{max} (ε/dm^3 mol^{-1} cm^{-1}): 554 (2400), 500 (5100), 439 (10700), 415 (11500), 340 (26000), 287 (34800) nm. Selected IR (solid) $\upsilon_{max} = 1607, 1512, 1445, 1348, 1248, 1174, 1109, 1013, 878, 835, 760, 559, 500$ cm^{-1}.

4.5.4. Synthesis of [Ir(**L4**)$_2$(bipy)][PF$_6$]

As [Ir(**L1**)$_2$(bipy)][PF$_6$] but with [(**L4**)$_2$Ir(μ-Cl$_2$)Ir(**L4**)$_2$] (100 mg, 0.09 mmol) and 2,2′-bipyridyl (16 mg, 0.11 mmol). Product collected as a red solid (27 mg, 21%). ^{1}H NMR (400 MHz, CDCl$_3$) δ_H 8.63 (d, $J = 4.64$ Hz, 2H), 8.45 (s, 2H), 8.43 (d, $J = 8.00$ Hz, 2H), 8.14 (app. t, $J = 9.28$ Hz, 2H), 7.87 (d, $J = 8.12$ Hz, 2H), 7.76 (m, 6H), 7.62 (s, 2H), 7.40 (dd, $J = 6.96, 8.12$ Hz, 2H), 7.32 (dd, $J = 5.80, 9.28$ Hz, 2H), 7.27 (s, 2H), 7.24 (s, 4H), 7.11 (d, $J = 8.52$ Hz, 2H), 6.94 (d, $J = 8.16$ Hz, 2H), 5.99 (s, 2H), 3.91 (s, 6H), 3.26 (s, 6H) ppm. ^{13}C{^{1}H} NMR (101 MHz, CDCl$_3$) δ_C 164.2, 161.4, 156.0, 148.2, 141.1, 137.2, 136.7,

136.2, 134.4, 134.0, 133.1132.1, 130.5, 128.9, 128.4, 128.1, 127.5, 125.6, 121.6, 119.8, 114.7, 108.3, 55.6, 54.8 ppm. HRMS found m/z 1131.3193; calcd m/z 1131.3209 for C$_{62}$H$_{46}$IrN$_6$O$_4$. UV-vis. (CHCl$_3$) λ_{max} (ε/dm^3 mol^{-1} cm^{-1}): 554 (10000), 455 (31700), 348 (55200), 285 (120700) nm. Selected IR (solid) $\upsilon_{max} = 1580, 1503, 1447, 1400, 1358, 1246, 1224, 1173, 1134, 1020, 978, 870, 837, 810, 772, 687, 519, 471$ cm^{-1}.

Appendix A. Supplementary data

Supplementary data to this article can be found online at https://doi.org/10.1016/j.jorganchem.2019.04.019. Information on the data underpinning the results presented here, including how to access them, can be found in the Cardiff University data catalogue at http://doi.org/10.17035/d.2019.0074136089.

References

[1] a C.-C. Hou, H.-M. Chen, J.-C. Zhang, N. Zhuo, Y.-Q. Huang, R.A. Hogg, D.T.D. Childs, J.-Q. Ning, Z.-G. Wang, F.-Q. Liu, Z.-Y. Zhang, Light Sci. Appl. 7 (2018) 17170;
b Y. Zhang, Y. Wang, J. Song, J. Qu, B. Li, W. Zhu, W.-Y. Wong, Adv. Optical Mater. 6 (2018) 1800466.
[2] X. Zhang, S. Bloch, W. Akers, S. Achilefu, Curr. Protoc. Cytom. 60 (2012), 12.27.1.
[3] a J.-C.G. Bünzli, C. Piguet, Chem. Soc. Rev. 34 (2005) 1048;
b S. Faulkner, S.J.A. Pope, B.P. Burton-Pye, Appl. Spectrosc. Rev. 40 (2005) 1;
c A.J. Amoroso, S.J.A. Pope, Chem. Soc. Rev. 44 (2015) 4723.
[4] a M.H.V. Werts, J.W. Hofstraat, F.A.J. Geurts, J.W. Verhoeven, Chem. Phys. Lett. 276 (1997) 196;
b L. Armelo, S. Quici, F. Barigelletti, G. Accorsi, G. Bottaro, M. Cavazzini, E. Tondello, Coord. Chem. Rev. 254 (2010) 487;
c A. Beeby, I.M. Clarkson, R.S. Dickens, S. Faulkner, D. Parker, L. Royle, A.S. de Sousa, J.A.G. Williams, M. Woods, J. Chem. Soc., Perkin Trans. 2 (1999) 493;
d A. Beeby, R.S. Dickins, S. Faulkner, D. Parker, J.A.G. Williams, Chem. Commun. (1997) 1401.
[5] a W. Levason, Coord. Chem. Rev. 340 (2017) 1;
b S.V. Eliseeva, J.-C.G. Bünzli, New J. Chem. 36 (2011) 1165;
c J.-C.G. Bünzli, Acc. Chem. Res. 39 (2006) 53.
[6] C. Wang, S. Otto, M. Dorn, E. Kreidt, J. Lebon, L. Srsan, P. Di Martino-Fumo, M. Gerhards, U. Resch-Genger, M. Seitz, K. Heinze, Angew. Chem. Int. Ed. 57 (2018) 1112.
[7] a S.D. Bergman, D. Gut, M. Kol, C. Sabatini, A. Barbieri, F. Barigelletti, Inorg. Chem. 44 (2005) 7943;
b B. Laramee-Milette, G.S. Hanan, Dalton Trans. 45 (2016) 12507;
c M.I.J. Polson, F. Loiseau, S. Campagna, G.S. Hanan, Chem. Commun. (2006) 1301;
d A. Damas, B. Ventura, J. Moussa, A.D. Esposti, L.-M. Chamoreau, A. Barbieri, H. Amouri, Inorg. Chem. 51 (2012) 1739.
[8] S. Silvi, E.C. Constable, C.E. Housecroft, J.E. Beves, E.L. Dunphy, M. Tomasulo, F.M. Raymo, A. Credi, Chem. Commun. (2009) 1484.
[9] a N. Su, F. Meng, P. Wang, X. Liu, M. Zhu, W. Zhu, S. Su, J. Yu, Dyes Pigments 138 (2017) 162;
b C.J. Adams, N. Fey, J.A. Weinstein, Inorg. Chem. 45 (2006) 6105;
c Y. Liu, W. Wu, J. Zhao, X. Zhang, H. Guo, Dalton Trans. 40 (2011) 9085;
d C.J. Adams, N. Fey, M. Parfitt, S.J.A. Pope, J.A. Weinstein, Dalton Trans. (2007) 4446.
[10] S. Kesarkar, W. Mroz, M. Penconi, M. Pasini, S. Destri, M. Cazzaniga, D. Ceresoli, P.R. Mussini, C. Baldoli, U. Giovanella, A. Bossi, Angew. Chem. Int. Ed. 55 (2016) 2714.
[11] P. Majumdar, X. Yuan, S. Li, B. Le Guennic, J. Ma, C. Zhang, D. Jacquemin, J. Zhao, J. Math. Chem. B 2 (2014) 2838.
[12] Z. Chen, L. Wang, C.-L. Ho, S. Chen, S. Suramitr, A. Plucksacholatarn, N. Zhu, S. Hannongbua, W.-Y. Wong, Adv. Optical Mater. 6 (2018) 1800824.
[13] H.-Y. Chen, C.-H. Yang, Y. Chi, Y.-M. Cheng, Y.-S. Yeh, P.-T. Chou, H.-Y. Hsieh, C.-S. Liu, S.-M. Peng, G.-H. Lee, Can. J. Chem. 84 (2006) 309.
[14] C. Wang, L. Lystrom, H. Yin, M. Hetu, S. Kilina, S.A. McFarland, W. Sun, Dalton

Trans. 45 (2016) 1636.
[15] a E.E. Langdon-Jones, A.J. Hallett, J.D. Routledge, D.A. Crole, B.D. Ward, J.A. Platts, S.J.A. Pope, Inorg. Chem. 52 (2013) 448;
b K.A. Phillips, T.M. Stonelake, K. Chen, Y. Hou, J. Zhao, S.J. Coles, P.N. Horton, S.J. Keane, E.C. Stokes, I.A. Fallis, A.J. Hallett, S.P. O'Kell, J.M. Beames, S.J.A. Pope, Chem. Eur J. 24 (2018) 8577.
[16] M. Nonoyama, Bull. Chem. Soc. Jpn. 47 (1974) 767.
[17] L.M. Groves, C. Schotten, J.M. Beames, J.A. Platts, S.J. Coles, P.N. Horton, D.L. Browne, S.J.A. Pope, Chem. Eur J. 23 (2017) 9407.
[18] Gaussian 09, Revision D. 01, M.J. Frisch, G.W. Trucks, H.B. Schlegel, G.E. Scuseria, M.A. Robb, J.R. Cheeseman, G. Scalmani, V. Barone, G.A. Petersson, H. Nakatsuji, X. Li, M. Caricato, A. Marenich, J. Bloino, B.G. Janesko, R. Gomperts, B. Mennucci, H.P. Hratchian, J.V. Ortiz, A.F. Izmaylov, J.L. Sonnenberg, D. Williams-Young, F. Ding, F. Lipparini, F. Egidi, J. Goings, B. Peng, A. Petrone, T. Henderson, D. Ranasinghe, V.G. Zakrzewski, J. Gao, N. Rega, G. Zheng, W. Liang, M. Hada, M. Ehara, K. Toyota, R. Fukuda, J. Hasegawa, M. Ishida, T. Nakajima, Y. Honda, O. Kitao, H. Nakai, T. Vreven, K. Throssell, J.A. Montgomery Jr., J.E. Peralta, F. Ogliaro, M. Bearpark, J.J. Heyd, E. Brothers, K.N. Kudin, V.N. Staroverov, T. Keith, R. Kobayashi, J. Normand, K. Raghavachari, A. Rendell, J.C. Burant, S.S. Iyengar, J. Tomasi, M. Cossi, J.M. Millam, M. Klene, C. Adamo, R. Cammi, J.W. Ochterski,

R.L. Martin, K. Morokuma, O. Farkas, J.B. Foresman, D.J. Fox, Gaussian, Inc., Wallingford CT, 2016.
[19] V. Barone, J. Bloino, M. Biczysko, F. Santoro, J. Chem. Theory Comput. 5 (2009) 540.
[20] F. Santoro, A. Lami, R. Improta, J. Bloino, V. Barone, J. Chem. Phys. 128 (2008) 224311.
[21] S.J. Coles, P.A. Gale, Chem. Sci. 3 (2012) 683.
[22] CrysAlisPro Software System, Rigaku Oxford Diffraction, 2015.
[23] L. Palatinus, G. Chapuis, J. Appl. Crystallogr. 40 (2007) 786—790.
[24] G.M. Sheldrick, Acta Crystallogr. Sect. C Struct. Chem. 71 (2015) 3.
[25] OLEX2: a complete structure solution, refinement and analysis program O.V. Dolomanov, L.J. Bourhis, R.J. Gildea, J.A.K. Howard, H. Puschmann, J. Appl. Crystallogr. 42 (2009) 339—341.
[26] D. Russell, Johnson III (Eds.), NIST Computational Chemistry Comparison and Benchmark Database, NIST Standard Reference Database Number 101, Release 19, April 2018. http://cccbdb.nist.gov/.
[27] Molecular graphics and analyses performed with UCSF Chimera, developed by the Resource for Biocomputing, Visualization, and Informatics at the University of California, San Francisco, with support from NIH P41-GM103311 E.F. Pettersen, T.D. Goddard, C.C. Huang, G.S. Couch, D.M. Greenblatt, E.C. Meng, T.E. Ferrin, J. Comput. Chem. 25 (2004) 1605.